

**Modeling of discontinuities in photonic crystal waveguides with the multiple multipole method**

Esteban Moreno,\* Daniel Erni, and Christian Hafner

*Laboratory for Electromagnetic Fields and Microwave Electronics, Swiss Federal Institute of Technology, ETH-Zentrum, Gloriastrasse 35, CH-8092 Zurich, Switzerland*

(Received 24 May 2002; published 27 September 2002)

A method for the simulation of discontinuities in photonic crystal defect waveguides is presented. This frequency domain technique is based on the multiple multipole method. In contrast with other known techniques, spurious reflections (due to the impedance mismatch at the waveguide terminations) are avoided. The absence of spurious reflections allows one to characterize precisely the intrinsic behavior of the sole discontinuity, reducing at the same time the size of the simulation domain. To achieve a perfect impedance matching, the guided modes of infinitely long waveguides corresponding to the input and output channels of the discontinuity are first computed using a supercell approach. Then, the discontinuity is fed with one of the previously computed modes, and the fields transmitted or reflected towards the discontinuity arms are matched to the modal fields corresponding to each output waveguide. This method allows one to compute the intrinsic transmission and reflection coefficients of the discontinuity (i.e., coefficients not altered by additional effects such as finite crystal size, etc.). The procedure is presented in detail using some simple discontinuities as test cases. Then, it is applied to the computation of the coupling from a waveguide to free space and for the analysis of a filtering  $T$  junction.

DOI: 10.1103/PhysRevE.66.036618

PACS number(s): 42.79.-e, 42.70.Qs, 42.82.-m, 02.60.Cb

**I. INTRODUCTION**

The design of integrated optical circuits has to face the problem of losses in waveguide bends and other interconnecting structures. In fact, the size of typical integrated optical components—containing bends, junctions, couplers, etc.—is of the order of millimeters or centimeters rather than micrometers due to the constraints imposed by the minimum radius of curvature of the interconnecting waveguides [1]. The increase of the dielectric contrast and the use of resonant cavities at waveguide corners [2] can reduce the losses, but it is difficult to suppress them completely.

In this framework, one of the most promising alternatives is the photonic crystal concept [3,4]. The underlying periodic structure of a photonic crystal gives rise to the appearance of frequency ranges (*photonic band gaps*) for which the optical field cannot propagate inside the crystal. This modification of the density of states of the optical field due to the periodicity of the crystal has many applications, e.g., it can provide alternative waveguiding schemes for dense integrated optics [1,5]. The disruption of the crystal periodicity by introduction of crystal defects induces a field localization that allows one to design various essential optical elements of very small size. For instance, line defects may behave as waveguides—for frequencies in the band gap—and, since the photons cannot escape through the crystal, waveguide corners with a radius of curvature of the order of one wavelength and without losses can be designed [6].

The basic building elements for the design of devices to modulate the optical field are essentially waveguide discontinuities. A waveguide discontinuity consists of several input and output channels that are connected by an interaction region [2]. The simplest photonic crystal waveguide disconti-

nities are bends [7–9], branches [10–12], and intersections [13]. They are prerequisites for the development of optical circuits in photonic crystals [14]. Much effort has been made recently for the analysis of sharp bends [13] (to allow for ultrasmall circuits) with the lowest possible reflection coefficient [7]. In this context, coupled-cavity waveguides seem to be quite promising [15]. The design of branching structures operating as power splitters [10,13], and of waveguide intersections without crosstalk [16,17] is also actively researched. Further structures (involving two different elements) are waveguides coupled to point defect microcavities [18–20], which can act as frequency discriminating systems [21]. Direct coupling of waveguides has been demonstrated for the design of directional couplers [22] and multiplexing systems [23], and indirect coupling via resonant cavities has been employed [24,25] for the design of channel drop filters. A proposal for multichannel wavelength division multiplexing [26] has been presented as well. To conclude, two last applications are mentioned, which concern the coupling to radiative modes (to be applied for the design of emitting antennas [27,28] and detectors [29]) and the important issue of the in coupling and out coupling of the modes guided by a photonic crystal line defect to a conventional waveguide [30–32] (operating as a sort of spot-size converter).

Up to now, the computation of photonic crystal waveguide discontinuities has been performed in time domain with the finite differences time-domain (FDTD) method (see, for instance, Ref. [7]) and with the time-domain beam propagation method [33], and in frequency domain with scattering matrix methods (see, for instance, Ref. [11]). However, as it will be explained in Sec. II, those methods have several drawbacks. Here, the goal is to present a general framework for the computation of photonic crystal waveguide discontinuities (in frequency domain) aiming at the following three aspects: (i) to avoid spurious reflections due to the impedance mismatching at the waveguide terminations, (ii) to char-

\*Electronic address: moreno@ifh.ee.ethz.ch

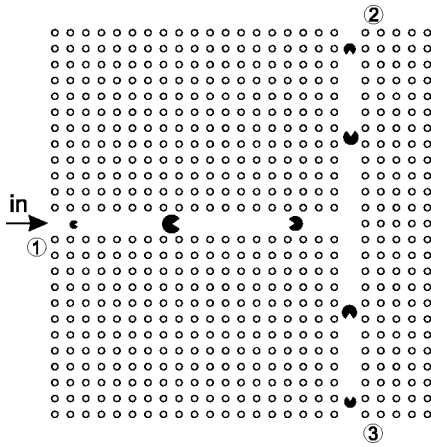


FIG. 1.  $T$  junction in a photonic crystal. The discontinuity is fed from the left. The “pacmen” represent the incident, transmitted, and reflected pulses (including the pulses reflected back at the crystal interfaces) at several different time instants.

acterize accurately the discontinuity, and (iii) to reduce the size of the computational domain. The presented technique is based on the multiple multipole (MMP) method [34] that is a well established semianalytical boundary method for the computation of electrodynamic problems.

Section II analyzes the drawbacks of the most commonly employed numerical techniques for the computation of photonic crystal discontinuities. Section III summarizes the basics of the MMP method. In Sec. IV the developed procedure is presented and its features are explained. Afterwards, in Sec. V, two applications are shown: a photonic crystal antenna and a  $T$  junction presenting a filtering behavior. The paper is closed with Sec. VI, where some conclusions are drawn.

## II. COMMONLY USED METHODS FOR THE SIMULATION OF PHOTONIC CRYSTAL WAVEGUIDE DISCONTINUITIES

The FDTD method has been successfully applied to the computation of various photonic crystal waveguide discontinuities. Some prominent examples are Refs. [7,10,24,31]. Here, the general advantages (such as easy modeling, etc.) and disadvantages (large memory requirements, etc.) of FDTD will not be discussed. Only those details specific for photonic crystal discontinuities are commented. The method is explained for the case of a  $T$  junction discontinuity (Fig. 1) in Ref. [10]. It proceeds in the following way: (i) The input waveguide ① is excited with a pulse (typically originated from a dipole in front of the input waveguide entrance) containing the relevant frequencies. (ii) The pulse propagates along the input waveguide towards the  $T$  junction. This waveguide has to be long enough to guarantee that the spatial transients due to the coupling in the waveguide have decayed before the pulse arrives to the discontinuity. (iii) The incident, transmitted, and reflected pulses are recorded and Fourier analyzed to determine the transmission [ $T_2(\omega)$  and  $T_3(\omega)$ ] and reflection [ $R(\omega)$ ] coefficients as a function of the frequency. Due to the finite size of the crystal, the pulses

arriving to the waveguide terminations ①, ②, and ③ after interacting with the junction are partially reflected back towards the junction. If these reflections are not carefully handled, they result in a complex mixture of the various transmitted and reflected pulses. To avoid this effect, two mechanisms have been proposed. The first one [10] consists in defining very long arms for the  $T$  junction. In this way, if the positions and the time windows where the pulses are recorded are properly chosen, the interferences between the various pulses are avoided. The second one makes use of sophisticated absorbing boundary conditions [35,36] to avoid spurious reflected pulses. The first approach requires huge computational domains (for instance, Ref. [10] reports on a computational domain of  $140 \times 180$  crystal cells), whereas the second approach has to ensure that the perfectly matched layers perform equally well for all incidence directions and all  $k$  wave numbers included in the wave packet.

In the frequency domain, scattering matrix methods have also been applied for the analysis of photonic crystal discontinuities [11,23,37]. As with FDTD, finite size crystals are simulated. The field inside the scattering cylinders is modeled with Bessel functions whereas the field outside the cylinders is represented by multipolar functions and one additional excitation function (usually a plane wave). In this case Fourier transformations are obviously not required, but on the other hand—as several authors have pointed out [11,15]—it is very difficult to determine the value of  $T_2(\omega)$ ,  $T_3(\omega)$ , and  $R(\omega)$ . The reason is again the reflection of the guided modes at the waveguides terminations: the field in each of the  $T$  junction branches is a superposition of waves transmitted or reflected at the junction itself and reflected at the waveguide termination (at the crystal interface). As a consequence, it is not easy to characterize precisely the intrinsic behavior of the sole discontinuity.

It is worth emphasizing the undesired effects that are introduced in the simulations with the mentioned methods due to the fact that finite crystals are modeled. The influence of the details of the waveguide termination and of the finite crystal size can be observed in the following two examples computed with MMP. In Fig. 2, it can be seen that the coupling to the waveguide is extremely sensitive to the fine details of the waveguide entrance: a very short tapering changes enormously the coupling efficiency of the incoming wave. The interference mentioned in the previous paragraph between the mode traveling downwards in the waveguide and the mode reflected back at the waveguide exit can be observed in Fig. 3(a). In this figure the field is compared with the pure modal field traveling downwards (i.e., without reflected mode) [Fig. 3(b)]. The mode in Fig. 3(b) was computed using the technique described in Ref. [38], appropriately generalized to consider the case of photonic crystal defects, namely, employing an adequate supercell.

## III. MULTIPLE MULTIPOLE METHOD

The MMP method [34,39] is a numerical technique for performing electrodynamic field calculations in the frequency domain (as usual, a factor  $e^{-i\omega t}$  multiplying the fields will not be explicitly written, where  $\omega$  is the angular

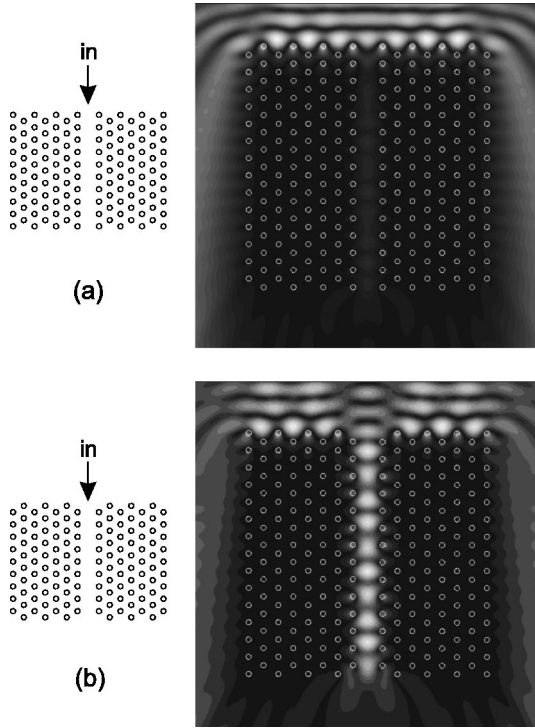


FIG. 2. Effect of “tapering” on the in-coupling behavior. The crystal considered here is a triangular lattice of dielectric ( $\epsilon_r = 8.41$ ) circular cross section cylinders in vacuum. The radius of the cylinders is  $r = 0.15a$ , where  $a$  is the lattice constant (the corresponding band structure is plotted in Fig. 12). The waveguide is excited with a plane wave incident from the top ( $E$  polarization) with normalized frequency  $\omega a / (2\pi c) = 0.473$  (which corresponds to an effective wavelength of  $\lambda_{\text{eff}} \approx 2.8a$  [see Fig. 13(a)]). The only difference between (a) and (b) is the row where the crystal is terminated. Observe that in (b) a kind of ultrashort tapering occurs, which enhances the in-coupling efficiency (the total power traveling downwards is approximately 26 times larger with taper than without it). The plotted field is the time averaged electric field.

frequency). It was developed for systems with isotropic, linear, and piecewise homogeneous materials, and its essential ideas are explained in the following. Since the structures considered in this paper are invariant along the  $Z$  axis, we present the MMP method for the two-dimensional (2D) case ( $\mathbf{r}$  will denote the position in the  $X$ - $Y$  plane, and a further factor  $e^{i\beta z}$  multiplying the fields will be omitted, where  $\beta$  is the propagation constant along the  $Z$  axis). However, this technique is not restricted to 2D problems.

The 2D region where the fields are to be computed is partitioned in domains  $\mathcal{D}_i$ , where the permittivity  $\epsilon^{\mathcal{D}_i}$  and permeability  $\mu^{\mathcal{D}_i}$  are  $\mathbf{r}$  independent (but, in general,  $\omega$  dependent). The field  $\Phi^{\mathcal{D}_i}(\mathbf{r})$  in every  $\mathcal{D}_i$  is expanded as a linear superposition of  $N^{\mathcal{D}_i}$  known analytical solutions  $\varphi_l^{\mathcal{D}_i}(\mathbf{r})$  of the 2D Helmholtz equation in the corresponding domain:

$$\begin{aligned} \Phi_{\text{approx}}^{\mathcal{D}_i}(\mathbf{r}) &= \Phi_{\text{exc}}^{\mathcal{D}_i}(\mathbf{r}) + \Phi_{\text{sca, approx}}^{\mathcal{D}_i}(\mathbf{r}) \\ &= \Phi_{\text{exc}}^{\mathcal{D}_i}(\mathbf{r}) + \sum_{l=1}^{N^{\mathcal{D}_i}} x_l^{\mathcal{D}_i} \varphi_l^{\mathcal{D}_i}(\mathbf{r}), \end{aligned} \quad (1)$$

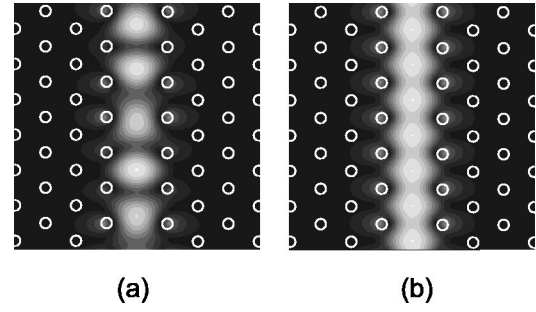


FIG. 3. Effect of the finite size of the crystal. The crystals in (a) and (b) have the same structure (described in Fig. 2). (a) Details of Fig. 2(b) for the seven central periods of the waveguide. (b) Modal field of an infinitely long waveguide computed with the supercell method. The pattern in (a) is due to the interference between the mode traveling downwards and the mode traveling upwards (reflected at the waveguide exit), whereas in (b) the field of the pure mode traveling downwards does not present such an effect. The plotted fields are the time averaged electric fields for  $\omega a / (2\pi c) = 0.473$ .

where  $\Phi^{\mathcal{D}_i}(\mathbf{r})$  denotes the approximation to the actual field,  $\Phi_{\text{exc}}^{\mathcal{D}_i}(\mathbf{r})$  and  $\Phi_{\text{sca, approx}}^{\mathcal{D}_i}(\mathbf{r})$  represent the exciting and approximated scattered fields, respectively, and  $x_l^{\mathcal{D}_i}$  are unknown coefficients to be determined.  $\Phi^{\mathcal{D}_i}(\mathbf{r})$  denotes a generic field from which the electric  $\mathbf{E}^{\mathcal{D}_i}(\mathbf{r})$  and magnetic  $\mathbf{H}^{\mathcal{D}_i}(\mathbf{r})$  fields can be extracted. In general, the knowledge of  $\Phi^{\mathcal{D}_i}(\mathbf{r}) = \{E_z^{\mathcal{D}_i}(\mathbf{r}), H_z^{\mathcal{D}_i}(\mathbf{r})\}$  is sufficient to derive the fields

$$\mathbf{E}_T^{\mathcal{D}_i}(\mathbf{r}) = \frac{i}{(\kappa^{\mathcal{D}_i})^2} [\beta \nabla_T E_z^{\mathcal{D}_i}(\mathbf{r}) - \omega \mu^{\mathcal{D}_i} (\mathbf{e}_z \times \nabla_T) H_z^{\mathcal{D}_i}(\mathbf{r})], \quad (2a)$$

$$\mathbf{H}_T^{\mathcal{D}_i}(\mathbf{r}) = \frac{i}{(\kappa^{\mathcal{D}_i})^2} [\beta \nabla_T H_z^{\mathcal{D}_i}(\mathbf{r}) + \omega \epsilon^{\mathcal{D}_i} (\mathbf{e}_z \times \nabla_T) E_z^{\mathcal{D}_i}(\mathbf{r})], \quad (2b)$$

where the subscript  $T$  denotes vectors in the  $X$ - $Y$  plane,  $\mathbf{e}_z$  is a unit vector along the  $Z$  axis, and  $\kappa^{\mathcal{D}_i}$  is the transverse wave vector:  $\epsilon^{\mathcal{D}_i} \mu^{\mathcal{D}_i} \omega^2 = (\kappa^{\mathcal{D}_i})^2 + \beta^2$ .

As the name of the method suggests, the multipolar functions are the most frequently used basis functions. A scalar 2D multipolar function with origin in the point  $\mathbf{r}_0$  is given by

$$\varphi_l^{\mathcal{D}_i}(r_l, \phi_l) = H_{n_l}^{(1)}(\kappa^{\mathcal{D}_i} r_l) \times \begin{cases} \cos(n_l \phi_l) \\ \sin(n_l \phi_l), \end{cases} \quad (3)$$

where  $H_{n_l}^{(1)}(\cdot)$  is the Hankel function of first kind and of order  $n_l$ , and  $(r_l, \phi_l)$  are polar coordinates with origin in  $\mathbf{r}_0$ . Usually, several “clusters” of multipolar functions are employed to expand the fields. Every cluster is a set of multipolar functions, all of them located at the same point and including several multipolar orders. We will call a *multipole expansion* of order  $n$  to such a cluster with orders  $n_l$  ranging from zero up to  $n$  [a *Bessel expansion* will be the same but

replacing the Hankel functions with Bessel functions  $J_{n_l}(\cdot)$ . Vekua theory [40] guarantees that for a multiply connected finite domain  $\mathcal{D}_i$ , one Bessel expansion and additionally a multipole expansion in each hole of  $\mathcal{D}_i$  form a complete basis. Nevertheless, when the interfaces  $\partial\mathcal{D}_{ij}$  of the domains deviate from the circular shape, several multipole expansions located at different positions achieve a much better convergence of the expansion in Eq. (1). Since a multipolar function is singular in its origin, the multipole expansions are placed outside  $\mathcal{D}_i$  to expand fields that are regular in  $\mathcal{D}_i$ .

To determine the unknown coefficients  $x_l^{D_i}$ , the boundary conditions are imposed on a set of collocation points  $\mathbf{r}_k$ ,  $k = 1, \dots, N_{\text{col}}$  along the interfaces  $\partial\mathcal{D}_{ij}$ :

$$\begin{aligned} w_{E_{\parallel}}(\mathbf{r}_k)[\mathbf{E}_{\parallel}^{D_i}(\mathbf{r}_k) - \mathbf{E}_{\parallel}^{D_j}(\mathbf{r}_k)] &= \mathbf{0}, \\ w_{E_{\perp}}(\mathbf{r}_k)[\varepsilon^{D_i} E_{\perp}^{D_i}(\mathbf{r}_k) - \varepsilon^{D_j} E_{\perp}^{D_j}(\mathbf{r}_k)] &= 0, \\ w_{H_{\parallel}}(\mathbf{r}_k)[\mathbf{H}_{\parallel}^{D_i}(\mathbf{r}_k) - \mathbf{H}_{\parallel}^{D_j}(\mathbf{r}_k)] &= \mathbf{0}, \\ w_{H_{\perp}}(\mathbf{r}_k)[\mu^{D_i} H_{\perp}^{D_i}(\mathbf{r}_k) - \mu^{D_j} H_{\perp}^{D_j}(\mathbf{r}_k)] &= 0, \end{aligned} \quad (4)$$

where  $\parallel$  and  $\perp$  stand for being tangential and orthogonal to the interface, respectively, and  $w_{(\dots)}(\mathbf{r}_k)$  are appropriately selected weights [34]. The system of Eq. (4) comprises  $6N_{\text{col}}$  equations in general or  $3N_{\text{col}}$  for  $H$  or  $E$  polarization and  $\beta = 0$ . The functions in Eq. (3) satisfy the radiation boundary conditions and therefore no special care is needed with this issue if they are used to represent the scattered field in open domains. System (4) leads to a rectangular (overdetermined) matrix equation of the type

$$\sum_{\beta} A_{\alpha\beta} X_{\beta} = B_{\alpha}, \quad (5)$$

where  $A_{\alpha\beta}$  is a rectangular matrix, the vector  $X_{\beta}$  includes the unknowns  $x_l^{D_i}$ , and the vector  $B_{\alpha}$  stems from the excitation. Equation (5) is solved in the least squares sense using a Givens algorithm [41]. The MMP method is claimed to be *semianalytical* because  $\Phi_{\text{approx}}^{D_i}(\mathbf{r})$  analytically satisfies the Maxwell differential equations in every  $\mathcal{D}_i$ , while the algebraic boundary conditions are approximately fulfilled at every  $\partial\mathcal{D}_{ij}$ . For further details, see Refs. [34,39].

The choice of the interfaces  $\partial\mathcal{D}_{ij}$ , which define the domains is often straightforward. Occasionally *fictional boundaries* (across which the material parameters do not change) are introduced in order to underpin a characteristic partitioning of the underlying problem, e.g., for convergence purposes [34]. The most difficult step in MMP modeling is the choice of the basis functions  $\varphi_l^{D_i}(\mathbf{r})$ . We have recently proposed a procedure for the automatic setting of the multipole expansions in 2D problems [42]. Once  $\partial\mathcal{D}_{ij}$  and  $\varphi_l^{D_i}(\mathbf{r})$  have been chosen, the selection of the collocation points  $\mathbf{r}_k$  is done in such a way that the multipolar functions with highest multipolar orders are sampled along the interfaces with a discretization that is fine enough [39].

An interesting feature of the MMP method is the possibility of evaluating the local accuracy of the computed solutions [34]. This can be measured by the *relative error* along the boundaries  $\partial\mathcal{D}_{ij}$ . The relative error is defined as the mismatch of the fields at the collocation points [i.e., the residual error in the fulfillment of Eq. (4)] divided by their values.

#### IV. MATCHING OF MODES AT WAVEGUIDE TERMINATIONS

##### A. General principle

From the discussion in Sec. II, it is clear that the main difficulty stems from the impedance mismatch at the waveguide terminations. This mismatch is what causes the undesired reflections. Therefore, the following procedure is proposed here (Fig. 4): The input and output waveguides are cut by planes ( $\pi_1$ ,  $\pi_2$ , and  $\pi_3$ ) at an appropriate distance from the discontinuity. Then, the fields going out from the junction are matched at the cutting planes to the modal fields [ $\Phi_{\text{in}}(\mathbf{r})$ ,  $\Phi_{\text{out}_1}(\mathbf{r})$ ,  $\Phi_{\text{out}_2}(\mathbf{r})$ , and  $\Phi_{\text{out}_3}(\mathbf{r})$ ] of the corresponding infinitely long waveguides. The procedure will be explained later in more detail, but let us anticipate that these modal fields of the input and output defect waveguides may be computed with any supercell approach. We computed these modes with a method based on MMP described elsewhere [38].

The proposed idea is routinely used for many applications where discontinuities in *conventional* (i.e., with continuous translational invariance) waveguides are present. In the context of the MMP method, it has been described for conventional metallic [43] (i.e., closed) and dielectric [44,45] (i.e., open) waveguides. However, to the best of our knowledge, the idea of defining input and output ports where the field is matched to the solution of the infinitely long waveguide, has not been employed for the computation of waveguides with *discrete* translational invariance. In comparison with the case of conventional waveguides, the application of the former idea to photonic crystals is more difficult. This is due to the fact that they possess only discrete translational symmetry, and to the fact that the energy waveguiding is not simple “index waveguiding,” but the more complex “distributed Bragg waveguiding,” which involves the scattering at a large number of elements. On the other hand, the analysis of open dielectric waveguide discontinuities can be more demanding due to the coupling to the continuous set of radiative modes. In this regard, photonic crystal waveguides are more akin to the metallic waveguides used in microwave applications, which strictly confine the electromagnetic field.

The main advantages of the idea presented above are the following: (i) Since a perfect matching of the guided modes is achieved, no spurious reflections occur at  $\pi_1$ ,  $\pi_2$ , and  $\pi_3$ , and it is possible to characterize the properties of the waveguide discontinuity alone. (ii) Complex (and not necessarily reliable) absorbing boundary conditions are avoided. (iii) No Fourier transformation is needed. (iv) The computational domain is reduced to the minimum possible size.

The procedure is now explained in detail. Figure 4(c) displays the domains and boundaries employed for the MMP

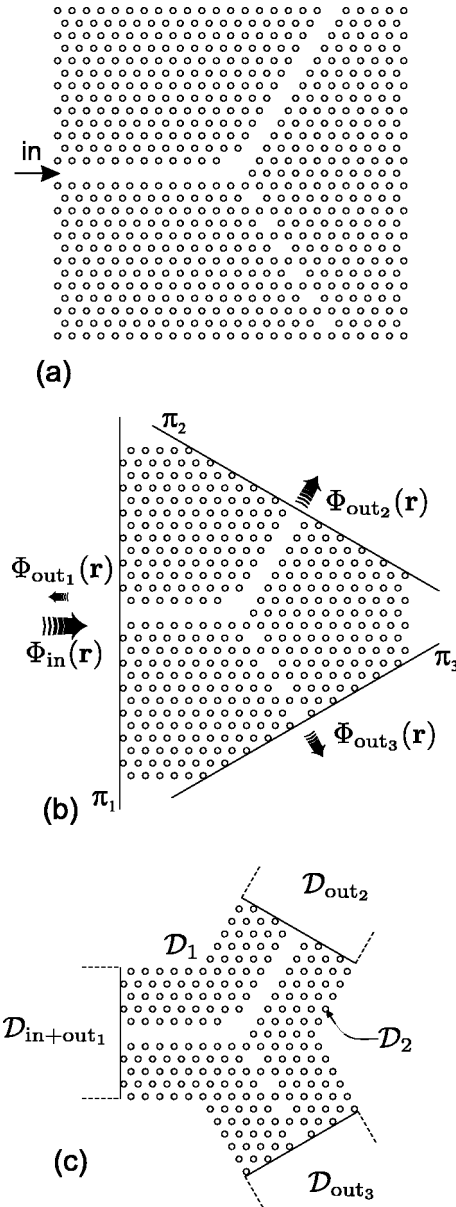


FIG. 4. (a) Typical photonic crystal discontinuity; three waveguides (two vacancy defect lines and one coupled-cavity waveguide) are connected to a central cavity. The Y junction is fed from the left. (b) For the simulation, the crystal is cut by planes  $\pi_1$ ,  $\pi_2$ , and  $\pi_3$ , and the fields arriving to those planes are matched to the modal fields  $[\Phi_{in}(\mathbf{r})$ ,  $\Phi_{out1}(\mathbf{r})$ ,  $\Phi_{out2}(\mathbf{r})$ , and  $\Phi_{out3}(\mathbf{r})$ ] of the corresponding infinitely long waveguides. (c) MMP domains and boundaries which are employed for the simulation (the dashed lines are only a visual help, and they are not used for the modeling).  $\mathcal{D}_1$  covers all the interaction region background, while  $\mathcal{D}_2$  covers the inner part of all cylinders.

simulation.  $\mathcal{D}_1$  and  $\mathcal{D}_2$  are the domains modeling the “interaction” region. The background is assigned to  $\mathcal{D}_1$  while the cylinders are assigned to  $\mathcal{D}_2$ . The boundaries  $\partial\mathcal{D}_{12}$  are the cylinder circumferences. There are three other domains ( $\mathcal{D}_{in+out1}$ ,  $\mathcal{D}_{out2}$ , and  $\mathcal{D}_{out3}$ ) corresponding to the input and output channels. Domains  $\mathcal{D}_1$  and  $\mathcal{D}_{in+out1}$ ,  $\mathcal{D}_{out2}$ ,  $\mathcal{D}_{out3}$  are separated by three fictitious boundaries (along the planes  $\pi_1$ ,

$\pi_2$ , and  $\pi_3$ ). The appropriate widths of the photonic crystal around the waveguides and the distances between discontinuity and in/out ports will be discussed in Sec. IV B. The fields in the different domains are modeled in the following way: In  $\mathcal{D}_1$  the field is represented by a multipole expansion at the center of each cylinder plus additional multipoles *inside* each of the in/out ports (along the three corresponding boundaries). In  $\mathcal{D}_2$  the field is modeled with Bessel expansions (one at the center of each cylinder; each such Bessel expansion represents the field only inside the corresponding cylinder). In each output port ( $\mathcal{D}_{out2}$  and  $\mathcal{D}_{out3}$ ) the field is modeled with the mode transmitted towards that port. Finally, in domain  $\mathcal{D}_{in+out1}$  the field is modeled with the incident and reflected modes (in the case that some waveguides are multimoded, additional modes are employed). Each modal field serving as input  $[\Phi_{in}(\mathbf{r})]$  or output  $[\Phi_{out1}(\mathbf{r})$ ,  $\Phi_{out2}(\mathbf{r})$ , and  $\Phi_{out3}(\mathbf{r})]$  mode is computed as in Ref. [38] with a supercell approach. Note that, in order to match the field in the interaction region to the guided modes in the in/out channels, it is only required to know the fields of the corresponding guided modes along the fictitious boundaries separating the interaction region  $\mathcal{D}_1$  and the in/out domains  $\mathcal{D}_{in+out1}$ ,  $\mathcal{D}_{out2}$ ,  $\mathcal{D}_{out3}$ .

It is important to realize that, since in the transition from the interaction region to the ports there is no impedance mismatch, the transmitted modes exiting towards  $\mathcal{D}_{out2}$  and  $\mathcal{D}_{out3}$  and the reflected mode exiting towards  $\mathcal{D}_{in+out1}$  are not reflected at the fictitious boundaries separating the in/out ports from the interaction region. This means that, when the input mode has amplitude 1, the (complex) amplitudes of the output modes—which are delivered by the MMP computation—are precisely the transmission  $[T_2(\omega), T_3(\omega)]$  and reflection  $[R(\omega)]$  coefficients of the discontinuity.

## B. Computational details and assessment of the method

There are several details that have not been commented yet. In what concerns the definition of the domains, three essential points are: (i) the number of photonic crystal layers around the defect waveguides and discontinuity center, (ii) the distances from the fictitious boundaries of the in/out ports to the discontinuity center, and (iii) the lengths of these fictitious boundaries. The photonic crystal waveguide employed for the examples shown in this section is described in Fig. 5, where a portion of the corresponding band structure is displayed.

The number of layers around the waveguide mentioned in point (i) has to guarantee a negligible leakage of the guided modes in its propagation through the discontinuity. On the other hand this number should be kept as small as possible to reduce the computational effort. In Fig. 4(c) the thickness of the photonic crystal surrounding the waveguide is equal to the length of the fictitious boundaries, but sometimes thicker photonic crystal walls are required (for instance, when high quality factor resonant cavities at the discontinuity have to be modeled). As a first assessment of the method, Fig. 6 displays the power transmission ( $|T|^2$ ) and reflection ( $|R|^2$ ) coefficients for a waveguide without discontinuity. The reflec-

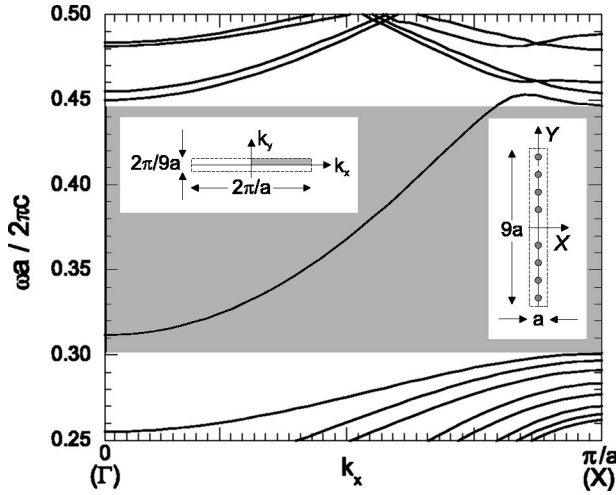


FIG. 5. Dispersion relation of the mode guided by a line of vacancies ( $E$  polarization). The insets show the first Brillouin zone (left) and the supercell (right). The shaded region represents the perfect crystal band gap. (The underlying employed perfect crystal consists in a square lattice with lattice constant  $a$ . The radius of the rods is  $r=0.18a$ . The background is vacuum and the relative permittivity of the rods is  $\epsilon_r=11.56$ ).

tion is 0 and the transmission is 1 except for low frequencies (corresponding to low wave numbers  $k$ , see Fig. 5). For low  $k$  the guided mode profile penetrates deeper in the photonic crystal, and therefore the leakage is higher. This loss of power can be diminished by adding more photonic crystal layers, as it is shown in Fig. 7: the addition of two more rows reduces the losses for low frequencies.

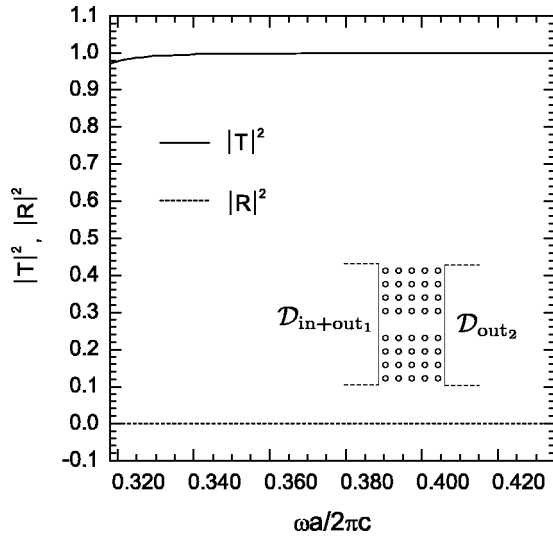


FIG. 6. Power transmission ( $|T|^2$ ) and reflection ( $|R|^2$ ) coefficients for a straight waveguide segment of length  $5a$  (where  $a$  is the lattice constant, see inset). The photonic crystal considered here is described in Fig. 5. The polarization is  $E$ , and the waveguide is a vacancy defect line. Observe that the reflection coefficient is 0 and the transmission is 1, except for the low frequencies (corresponding to low wave numbers  $k$  and wide modal profiles penetrating deeply in the photonic crystal).

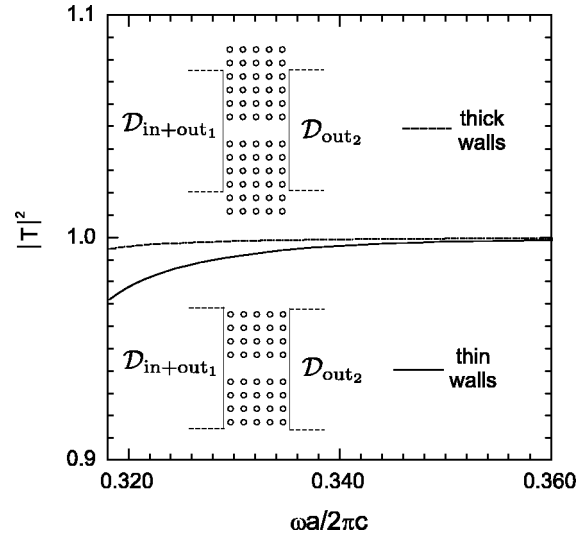


FIG. 7. Power transmission coefficients for a straight waveguide segment with photonic crystal walls of different thicknesses (see insets). The losses observed in Fig. 6—for low frequencies—are reduced by adding two further photonic crystal layers.

The distances between the ports and the discontinuity center mentioned in (ii) should be as short as possible in order to reduce the size of the computational window and, hence, the numerical effort. However, since the fields going out from the junction will be matched to pure guided modes at the ports, these distances should be long enough to guarantee that the fields arriving at the fictitious boundaries are pure guided modes and the spatial evanescent terms have already faded away. It is worth noting that these distances depend on the effective wavelength of the guided mode and, therefore, they have to be longer for low  $k$  wave number. This is shown in Figs. 8 and 9(a), which display the power transmission and reflection coefficients due to a  $90^\circ$  bend in a vacancy line defect. In Fig. 8 the power is not conserved—for low frequencies—because the lengths of the bend arms are too short for the corresponding effective wavelengths and the evanescent transients reach the in/out ports. Note that the conservation of energy deteriorates for  $\omega a / (2\pi c) < 0.370$ , which corresponds to (see Fig. 5)  $k_x \approx 0.5\pi/a$ , i.e., an effective wavelength of  $\lambda_{\text{eff}} = 2\pi/k_x \approx 4a$ . This is approximately the length of the bend arms employed in the simulation (see inset of Fig. 8). Increasing the length of the arms, the frequency range for which the model works properly is extended to lower frequencies [Fig. 9(a)]. As a rule, the length of the waveguide arms should be at least one effective wavelength of the guided mode for the operating frequency. The same structure was computed with FDTD [7] using a simulation domain 50 times larger than the domain employed in Fig. 9 [53]. The small inaccuracy of the energy conservation observed in Fig. 8 for high frequencies is due to the fact that those frequencies are very close to the band gap edge and the leakage is higher. This can be avoided by addition of one layer of photonic crystal [Fig. 9(a)]. The inaccuracy in the power conservation then becomes smaller than 0.2% of the input power. The field in the bend is plotted in Fig. 9(b).

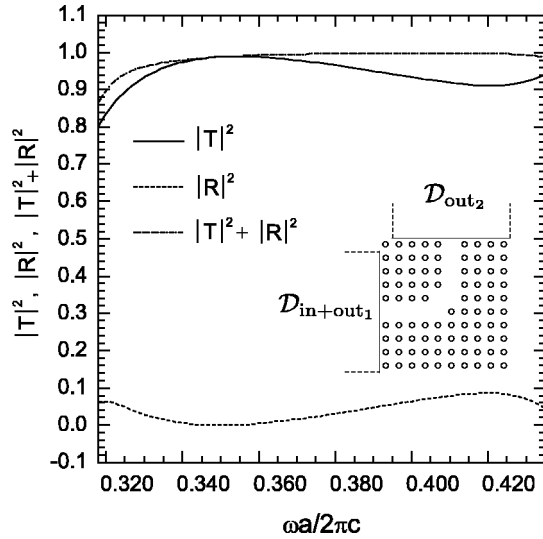


FIG. 8. Power transmission ( $|T|^2$ ) and reflection ( $|R|^2$ ) coefficients for a  $90^\circ$  bend with arms of an approximate length of  $4a$  (where  $a$  is the lattice constant, see inset). The photonic crystal considered here is the same as in Fig. 5. Observe that the total power is not well conserved for low and for high frequencies. For low frequencies (corresponding to long effective wavelengths) the bend arms are too short and the spatial transients reach the in/out ports. For high frequencies the mode frequency is very close to the band edge and the mode is less well confined in the defect waveguide (note that this effect does not occur for low frequencies because the mode does not cross the lower band edge, see Fig. 5).

Finally, the lengths of the fictitious boundaries of the ports mentioned in (iii) should guarantee that the guided mode amplitude is negligible at both end points of the fictitious boundary. Usually this length is the same as that of the supercell employed to determine the modal guided fields. Note again that the modes penetrate deeper in the photonic crystal for low  $k$ , which means that larger supercells are required, and correspondingly longer fictitious boundaries.

Regarding the expansions modeling the fields, one should pay attention to the following points. (a) In this paper only circular cross section cylinders have been considered. For this case, one Bessel expansion plus one multipole expansion (both located at each cylinder center) are probably optimal. For other geometries more expansions may be needed [38]. (b) The multipole expansions located inside the in/out ports and radiating towards  $\mathcal{D}_1$  are positioned equidistant from each other and from the corresponding fictitious boundaries. (c) The maximum order of the expansions mentioned in the two previous points depends on the desired accuracy. As it could be expected, those expansions close to the defect waveguides and to the central cavity are more important and should usually have a higher order.

The numerical details of the computations shown in Fig. 9 are summarized as follows: 208 multipole expansions were employed for domain  $\mathcal{D}_1$  (one multipole inside each cylinder and additionally nine in  $\mathcal{D}_{\text{in+out}_1}$  and nine in  $\mathcal{D}_{\text{out}_2}$ ) and 190 Bessel expansions for domain  $\mathcal{D}_2$  (one per cylinder). The order of the expansions is  $n=3$  except in two cases: those inside the cylinders that are nearest neighbors to the vacancy

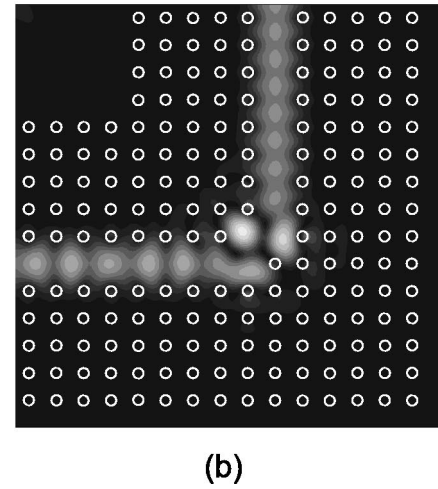
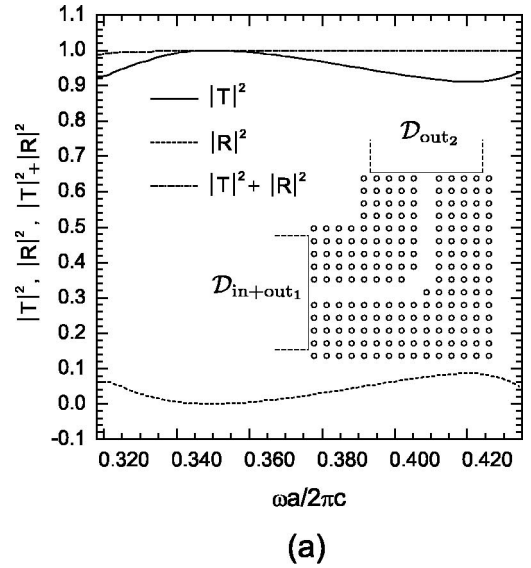


FIG. 9. (a) Power transmission ( $|T|^2$ ) and reflection ( $|R|^2$ ) coefficients for a  $90^\circ$  bend with arms of an approximate length of  $7.5a$  (where  $a$  is the lattice constant, see inset). Observe that the total power is now conserved for  $\omega a/(2\pi c) > 0.325$ . (b) Time-averaged electric field for  $\omega a/(2\pi c) = 0.435$ . In the horizontal branch the interference between the incoming and reflected modes can be observed, whereas in the vertical branch only a pure transmitted mode propagates. The bend is fed from the left.

defects (where  $n=5$  was required) and those that are second nearest neighbors (with  $n=4$ ). The total number of basis functions adds up to 3265 ( $N^{\mathcal{D}_1} = 1710$ ,  $N^{\mathcal{D}_2} = 1552$ ,  $N^{\mathcal{D}_{\text{in+out}_1}} = 2$ ,  $N^{\mathcal{D}_{\text{out}_2}} = 1$ ). The average relative error along the boundaries for the computation shown in Fig. 9(b) was 0.25% (not to be confused with the inaccuracy in the power conservation of 0.2% mentioned above) and the maximum relative error was 16%. The absolute errors are of similar magnitude in all collocation points, and the mentioned maximum relative error occurs in collocation points lying far from the channel where the energy is guided, i.e., in collocation points where the field is almost zero and therefore, despite the high accuracy, it is very difficult to obtain low relative errors for them. Up to now we have not found any

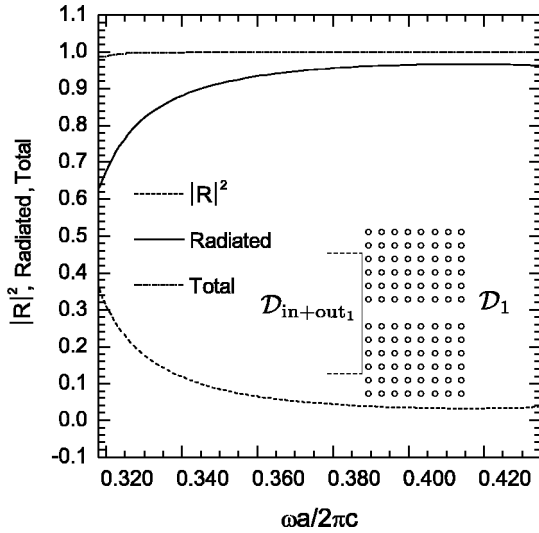


FIG. 10. Reflected ( $|R|^2$ ), radiated, and total power for a transition between a defect waveguide and free space. The photonic crystal considered here is the same as in Fig. 5. The length of the waveguide before the discontinuity is approximately  $7.5a$ . That means (see Fig. 5) that the model should deteriorate for  $\omega a/(2\pi c) < 0.325$ , as it is indeed observed in the figure (see the total power curve).

simple quantitative relation between the relative error in the collocation points and the inaccuracy in the power conservation. However, collocation errors are usually an upper bound of the error quantities involved. Moreover, the availability of a quantitative error measure (i.e., the relative error distribution) provides a very useful validation tool.

## V. APPLICATIONS

### A. Coupling to radiative modes

The discontinuities considered in Sec. IV B were closed, i.e., the whole structure is surrounded by photonic crystal layers (infinitely thick in the ideal case) and therefore no energy should leak out of the system. Nevertheless, the generalization to open systems is not conceptually difficult, although it is more demanding from the modeling point of view. In this section the coupling from the waveguide to free space and the effects of the termination of photonic crystal waveguides at the crystal interface are considered. It has been already mentioned (Fig. 2) that the fine details of the waveguide termination have a crucial importance in the coupling of the guided modes to the radiation modes. However, with conventional scattering matrix computations this effect could not be quantified because the mode arriving at the interface (from the source) and the mode reflected at the interface back towards the source are mixed.

The method described in Sec. IV can be applied to this kind of discontinuity between waveguide and free space. Here, only one port for guided modes ( $\mathcal{D}_{\text{in}+\text{out}_1}$ ) is needed (inset of Fig. 10) whereas the radiation couples out in domain  $\mathcal{D}_1$ . Except under special conditions (when surface modes are excited) the elements described in Sec. IV are enough for the modeling of this type of discontinuity. The

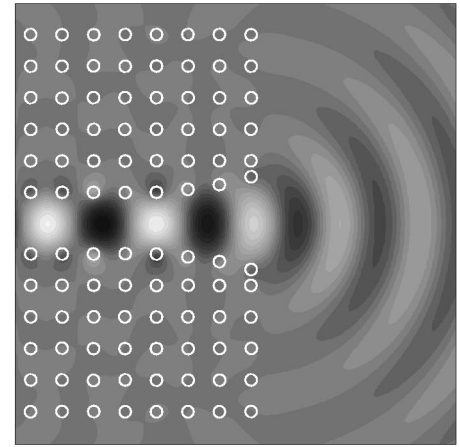
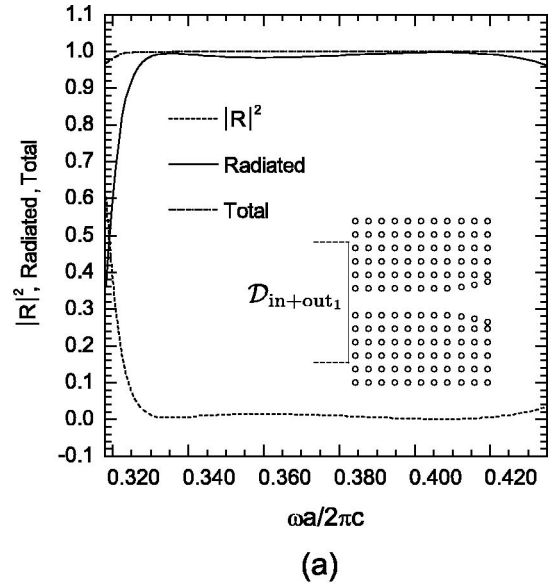


FIG. 11. (a) Reflected ( $|R|^2$ ), radiated, and total power for a transition between a defect waveguide and free space. The photonic crystal considered here is the same as in Fig. 5. The tapering decreases the reflection coefficient significantly. Due to the short length of the waveguide tract, the simulation results are not correct for low frequencies  $\omega a/(2\pi c) < 0.325$  (as it was discussed in Sec. IV B). (b) Electric field amplitude radiated by the tapered waveguide. The normalized frequency is  $\omega a/(2\pi c) = 0.395$ .

number of photonic crystal layers around the waveguide has to be enough to ensure a good modal confinement, and additionally it has to be such that the outgoing field does not “feel” the finite lateral size of the crystal. It may be useful to mention that the field in domain  $\mathcal{D}_1$  is expanded exactly in the same way as in Sec. IV: One multipole expansion inside each cylinder plus a set of multipole expansions inside  $\mathcal{D}_{\text{in}+\text{out}_1}$ .

Figures 10 and 11(a) show the reflected ( $|R|^2$ ), radiated, and total power (reflected plus radiated) for two different waveguide terminations (see insets). Observe the good energy conservation (better than 0.5%) except for very low frequencies (this effect has already been discussed in

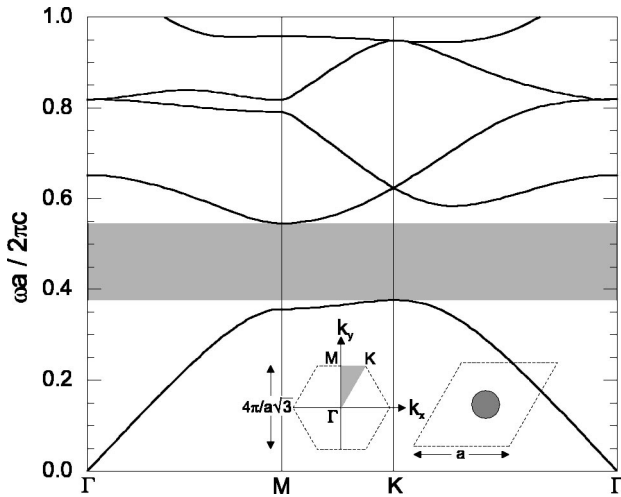


FIG. 12. Band structure of a triangular lattice of dielectric ( $\epsilon_r = 8.41$ ) circular cross section cylinders in vacuum. The radius of the cylinders is  $r=0.15a$ , where  $a$  is the lattice constant. The polarization is  $E$ . The insets show the first Brillouin zone (left) and the primitive cell (right).

Sec. IV B); to obtain correct results for lower frequencies, a longer piece of waveguide has to be simulated. It is also important noticing that the reflection coefficient has been significantly decreased in most of the frequency range by introduction of a short tapering [Fig. 11(a)]. Compared to conventional waveguide tapers, here the radiation coupling seems nearly perfect, underlining the peculiarities of photonic crystal tapers. The electric field in the structure is plotted in Fig. 11(b).

**B. Filtering  $T$  junction**

In this section a complex  $T$  junction discontinuity of the generic type shown in Fig. 4 is analyzed. In the structure considered here the three in/out waveguides are different from each other. The underlying photonic crystal is a triangular lattice of dielectric cylinders in air, and it has the band structure depicted in Fig. 12. The diagram shows a wide band gap between the first and second bands.

Many different line defects can be introduced in this crystal. Some of them (with the corresponding dispersion relations) are summarized in Fig. 13. Usually, line defects preserving the symmetry of the crystal [such as Figs. 13(a) and 13(b)] are preferred [46], and most studies in the literature focus on this type of waveguides. The reason is that, since the underlying global lattice is not disrupted, the design of complex photonic circuits is, in principle, easier. However, other kinds of waveguides which disrupt the underlying lattice have been studied [47], e.g., stacking faults. Two examples of such defects are shown in Figs. 13(c) and 13(d). The modes labeled (a) and (c) present a very similar behavior except close to the Brillouin zone edge: the (c) mode is degenerated whereas (a) is not (this effect was also found in Ref. [47]). Here, it will be shown that stacking faults can be used to design devices with interesting functionalities.

The discontinuity considered in this section is shown in Fig. 14. The figure caption describes in detail how the  $T$

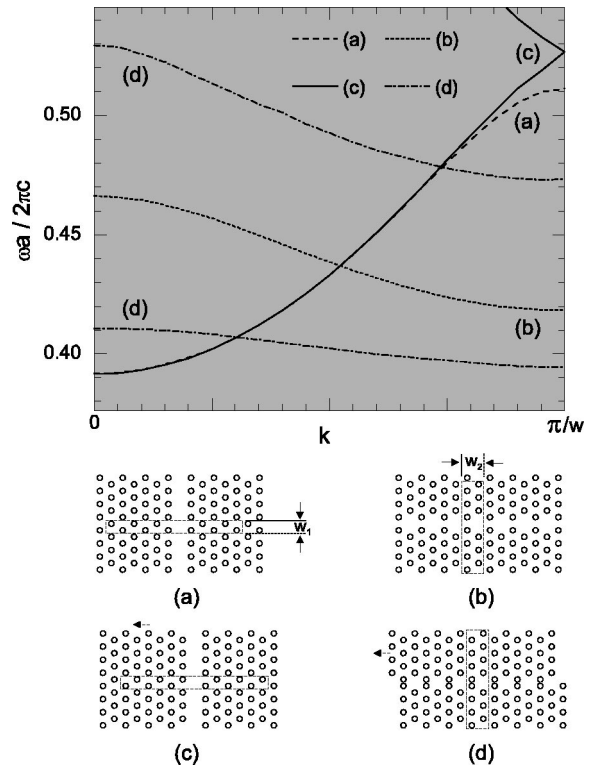


FIG. 13. Dispersion relation for several defect waveguides in the crystal described in Fig. 12 (note that the horizontal axis is normalized using the width  $w$  of the supercell, which is not the same for all waveguides). (a) and (b) are vacancy line defects obtained by removing one column and one row of cylinders, respectively [in fact, (b) behaves like a coupled-cavity waveguide]. (c) and (d) are obtained by sliding two parts of the crystal with respect to each other by a distance  $a\sqrt{3}/2$ . In (c) a channel waveguide with dispersion similar to (a) is obtained whereas in (d) a coupled-cavity waveguide (two moded in the whole  $k$  range) results.

junction is constructed. Two waveguides are created by sliding a piece of the photonic crystal, whereas the third one is built by removing one row of cylinders. As a byproduct of this construction, a cavity appears at the center of the  $T$  junction. From the figure, it is intuitive that the right and left

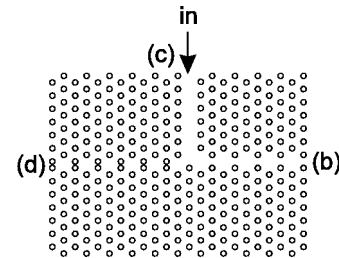
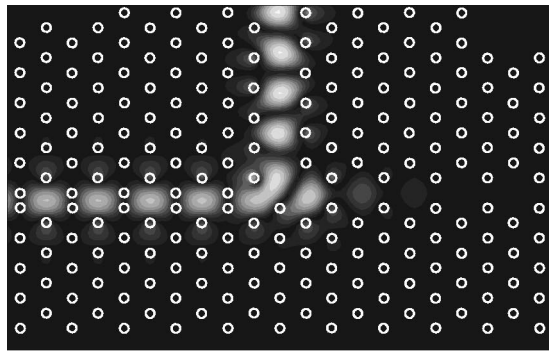
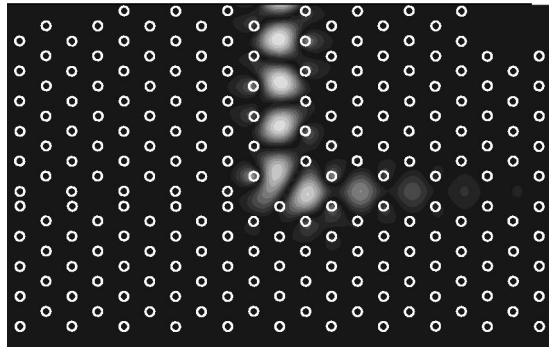


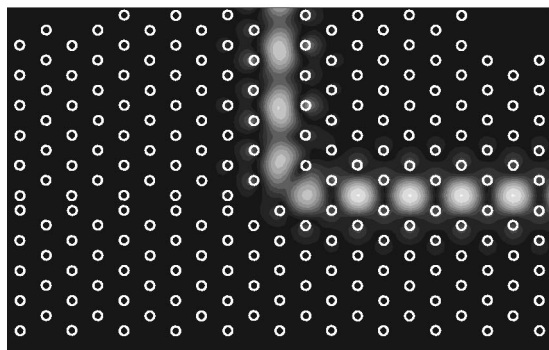
FIG. 14.  $T$  junction with filtering behavior (diplexer). The structure is based on the perfect crystal described in Fig. 12. Two waveguides [of types (c) and (d), see Fig. 13] are obtained by sliding the upper left block of the crystal by a distance  $a\sqrt{3}/2$ . The third waveguide [of type (b)] is a coupled-cavity waveguide obtained by removing a row of adjacent cylinders. At the intersection a cavity is formed, which consists of two smaller subcavities (of sizes similar to as those at the left and right of the junction).



$$\omega a / (2\pi c) = 0.478$$



$$\omega a / (2\pi c) = 0.470$$



$$\omega a / (2\pi c) = 0.437$$

FIG. 15. Filtering behavior of the  $T$  junction structure shown in Fig. 14. The plotted field is the time averaged electric field.

waveguides will behave as coupled-cavity waveguides. This kind of waveguide presents flattened bands, and therefore its bandwidth is small. The bandwidth depends on the coupling between the cavities, becoming smaller for weak coupling [15,48]. Since the cavities constituting the right waveguide (b) are larger than those of the left waveguide (d), the defect band of the right one will have lower frequencies compared to that of the left one. In addition, the vertical channel (c) will support modes for a larger range of frequencies. If the frequency range of (c) overlaps with those of (b) and (d), this could be used to implement a  $T$  junction, which additionally filters one low frequency towards the right and one high frequency towards the left. In fact, in Fig. 13, this kind of desired overlapping band behavior is precisely observed.

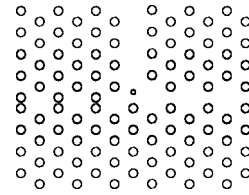
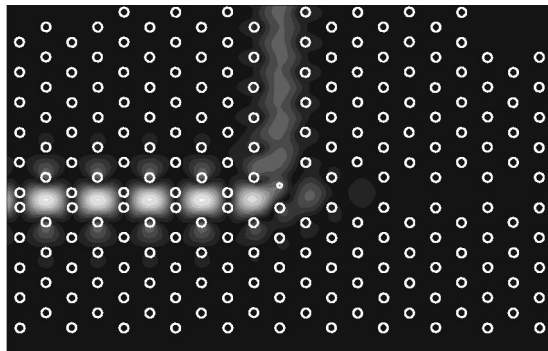


FIG. 16. Improved  $T$  junction with filtering behavior. The structure is the same as described in Fig. 14 with addition of one further rod at the junction. The radius of this rod is  $r' = r/2$  (where  $r$  is the radius of the other rods), and it is positioned at a distance  $3a/4$  from the rod immediately below. By choosing the position and radius of this rod, the modes of the central cavity can be appropriately manipulated. The domain employed for the simulations has a size of 10 lattice constants in the vertical direction. In the horizontal direction the domain contains the central  $\infty$ -shaped cavity plus four cavities at each side of it.

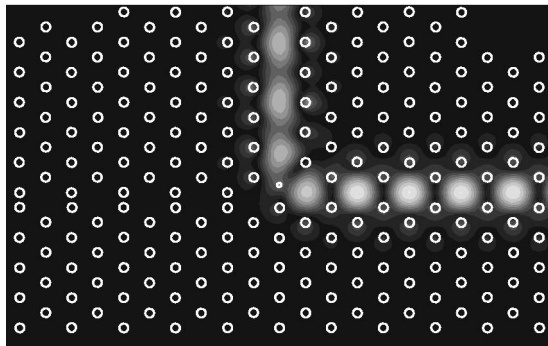
From the analysis of the dispersion curves in Fig. 13 it is clear that for the frequency  $\omega a / (2\pi c) \approx 0.437$  [respectively  $\omega a / (2\pi c) \approx 0.478$ ] transmission from the top to the right (respectively left) waveguide should be possible. In the intermediate frequency range [for  $\omega a / (2\pi c) \approx 0.470$ ] none of the horizontal waveguides supports propagating modes and therefore total reflection is expected. It is worth noting that by simple lattice operations (dislocation and cylinders removal) the functionality of a diplexer is achieved.

For the simulation of this device, the ideas explained in Sec. IV were followed. The only new ingredients are: (i) Each waveguide supports different modes, and therefore the corresponding different fields have to be matched at each in/out port. (ii) Since the slope of the dispersion relation is negative for the coupled-cavity modes, the group velocity is negative. The sign of the wave number  $k$  has to be chosen appropriately in order to obtain the correct direction for the energy propagation. (iii) The vertical defect waveguide supports a guided mode for all considered frequencies, but this is not the case for the horizontal waveguides. This means that for certain frequencies, no propagating mode is available to match the field at the right or at the left port. For those frequencies which do not support a mode either to the right or to the left, the corresponding branch of the  $T$  junction is left “open,” i.e., no output port is attached at the end of the waveguide (taking care that the arm is long enough so that no power leaks out, and the reflection coefficient is not modified).

As the previous considerations predicted, Fig. 15 shows the filtering behavior of the  $T$  junction. The power transmitted to the corresponding branches for the considered frequencies is 35% (towards the left, for the high frequency) and 87% (towards the right for the low one). To achieve a higher transmission for both frequencies, the central cavity has to be redesigned, in such a way that it possesses two modes, and the coupling coefficients of those modes with the adjacent waveguides are appropriate [10,25,49–51]. The idea is to find a cavity with the following properties: (i) The right (respectively left) subcavity has the same resonant frequency as the right (respectively left) waveguide. (ii) The coupling factor of the right (respectively left) subcavity to the left (respectively right) waveguide is negligible. (iii) The decay



$$\omega a / (2\pi c) = 0.478$$



$$\omega a / (2\pi c) = 0.437$$

FIG. 17. Filtering behavior of the modified  $T$  junction structure with the additional rod in the central cavity (Fig. 16). The plotted field is the time averaged electric field. Here, in contrast with Fig. 15, almost no interference pattern in the vertical input waveguide is observed, which indicates that the reflection coefficients are smaller.

rates of the mode sustained by the right (respectively left) subcavity to the upper and to the right (respectively left) waveguides are the same. Points (i) and (ii) enforce the filtering behavior, whereas (iii) minimizes the reflections back

towards the input waveguide (for the chosen resonant frequencies). The optimization of the cavity in order to satisfy the previous requirements will not be presented here. Nevertheless, to make it plausible, the following experiment is considered: In the central cavity one additional rod is included (Fig. 16). Adjusting the radius  $r'$  and position of this column by trial and error, the power transmitted towards the left is 98.8% for the high frequency and 93.3% towards the right for the low frequency, just demonstrating the potentialities of such intervention (the inaccuracy in the energy conservation was smaller than 1%). The time averaged electric field corresponding to this configuration is plotted in Fig. 17. Observe that the interference pattern in the input waveguide has almost disappeared (especially for the high frequency), which means that the reflection coefficients are very small.

## VI. CONCLUSIONS

Photonic crystal waveguide discontinuities can be accurately characterized with the presented method. Since the fields traveling away from the discontinuity are matched to the guided modes supported by the output channels, no spurious reflections occur. Thus, the computed transmission and reflection coefficients are due to the discontinuity alone, and finite crystal size effects are not mixed with the intrinsic discontinuity behavior. Additionally, the size of the computational domain required for the simulation can be reduced to the minimum possible. The approach has been demonstrated within the context of coupling to radiative modes, power splitting, and diplexer operation. Extended versions of MMP for three-dimensional modeling are already available [52], but their efficiency concerning photonic crystal simulations has not been evaluated yet.

## ACKNOWLEDGMENTS

This work was supported by the Swiss National Science Foundation and by the Swiss Center for Electronics and Microtechnology.

- 
- [1] T.F. Krauss and R.M. De La Rue, *Progress Quantum Electron.* **23**, 51 (1999).
  - [2] C. Manolatu, S.G. Johnson, S. Fan, P.R. Villeneuve, H.A. Haus, and J.D. Joannopoulos, *J. Lightwave Technol.* **LT17**, 1682 (1999).
  - [3] E. Yablonovitch, *Phys. Rev. Lett.* **58**, 2059 (1987).
  - [4] S. John, *Phys. Rev. Lett.* **58**, 2486 (1987).
  - [5] G. Parker and M. Charlton, *Phys. World* **13**(8), 29 (2000).
  - [6] S.-Y. Lin, E. Chow, V. Hietala, P.R. Villeneuve, and J.D. Joannopoulos, *Science* **282**, 274 (1998).
  - [7] A. Mekis, J.C. Chen, I. Kurland, S. Fan, P.R. Villeneuve, and J.D. Joannopoulos, *Phys. Rev. Lett.* **77**, 3787 (1996).
  - [8] A. Mekis, S. Fan, and J.D. Joannopoulos, *Phys. Rev. B* **58**, 4809 (1998).
  - [9] A. Chutinan and S. Noda, *Phys. Rev. B* **62**, 4488 (2000).
  - [10] S. Fan, S.G. Johnson, J.D. Joannopoulos, C. Manolatu, and H.A. Haus, *J. Opt. Soc. Am. B* **18**, 162 (2001).
  - [11] J. Yonekura, M. Ikeda, and T. Baba, *J. Lightwave Technol.* **LT17**, 1500 (1999).
  - [12] T. Baba, N. Fukaya, and J. Yonekura, *Electron. Lett.* **35**, 654 (1999).
  - [13] T. Sondergaard and K.H. Dridi, *Phys. Rev. B* **61**, 15 688 (2000).
  - [14] A.R. McGurn, *Phys. Rev. B* **61**, 13 235 (2000).
  - [15] A. Boag and B.Z. Steinberg, *J. Opt. Soc. Am. A* **18**, 2799 (2001).
  - [16] S.G. Johnson, C. Manolatu, S. Fan, P.R. Villeneuve, J.D. Joannopoulos, and H.A. Haus, *Opt. Lett.* **23**, 1855 (1998).
  - [17] E. Centeno and D. Felbacq, *J. Opt. A: Pure Appl. Opt.* **3**, S154 (2001).
  - [18] P.R. Villeneuve, D.S. Abrams, S. Fan, and J.D. Joannopoulos, *Opt. Lett.* **21**, 2017 (1996).
  - [19] M. Agio, E. Lidorikis, and C.M. Soukoulis, *J. Opt. Soc. Am. B* **17**, 2037 (2000).

- [20] S. Noda, A. Chutinan, and M. Imada, *Nature (London)* **407**, 608 (2000).
- [21] R. Stoffer, H.J.W.M. Hoekstra, R.M. de Ridder, E. Van Groesen, and F.P.H. Van Beckum, *Opt. Quantum Electron.* **32**, 947 (2000).
- [22] M. Tokushima and H. Yamada, *Electron. Lett.* **37**, 1454 (2001).
- [23] E. Centeno, B. Guizal, and D. Felbacq, *J. Opt. A: Pure Appl. Opt.* **1**, L10 (1999).
- [24] S. Fan, P.R. Villeneuve, J.D. Joannopoulos, and H.A. Haus, *Phys. Rev. Lett.* **80**, 960 (1998).
- [25] S. Fan, P.R. Villeneuve, J.D. Joannopoulos, M.J. Khan, C. Manolatu, and H.A. Haus, *Phys. Rev. B* **59**, 15 882 (1999).
- [26] A. Sharkawy, S. Shi, and D.W. Prather, *Appl. Opt.* **40**, 2247 (2001).
- [27] C.R. Simovski and S. He, *Microwave Opt. Technol. Lett.* **31**, 214 (2001).
- [28] M. Qiu and S. He, *Phys. Lett. A* **282**, 85 (2001).
- [29] S.A. Magnitskii, A.V. Tarasishin, and A.M. Zheltikov, *Appl. Phys. B: Lasers Opt.* **B69**, 497 (1999).
- [30] A. Mekis and J.D. Joannopoulos, *J. Lightwave Technol.* **LT19**, 861 (2001).
- [31] Y. Xu, R.K. Lee, and A. Yariv, *Opt. Lett.* **25**, 755 (2000).
- [32] T.D. Happ, M. Kamp, and A. Forchel, *Opt. Lett.* **26**, 1102 (2001).
- [33] M. Koshiba, Y. Tsuji, and M. Hikari, *J. Lightwave Technol.* **LT18**, 102 (2000).
- [34] C. Hafner, *Post-modern Electromagnetics. Using Intelligent Maxwell Solvers* (Wiley, Chichester, 1999).
- [35] A. Mekis, S. Fan, and J.D. Joannopoulos, *IEEE Microwave Guid. Wave Lett.* **9**, 502 (1999).
- [36] M. Koshiba, Y. Tsuji, and S. Sasaki, *IEEE Microwave Wireless Components Lett.* **11**, 152 (2001).
- [37] G. Tayeb and D. Maystre, *J. Opt. Soc. Am. A* **14**, 3323 (1997).
- [38] E. Moreno, D. Erni, and C. Hafner, *Phys. Rev. B* **65**, 155120 (2002).
- [39] C. Hafner, *The Generalized Multipole Technique for Computational Electromagnetics* (Artech House, Boston, 1990).
- [40] I.N. Vekua, *New Methods for Solving Elliptic Equations* (North-Holland, Amsterdam, 1967).
- [41] G.H. Golub and C.F. Van Loan, *Matrix Computations* (Johns Hopkins University Press, Baltimore, 1996).
- [42] E. Moreno, D. Erni, C. Hafner, and R. Vahldieck, *J. Opt. Soc. Am. A* **19**, 101 (2002).
- [43] C. Hafner, *Int. J. Numer. Model.* **3**, 247 (1990).
- [44] C. Hafner, in *Proceedings of the Fourth Conference on Electromagnetic and Light Scattering by Nonspherical Particles: Theory and Applications*, edited by F. Obelleiro, J.L. Rodríguez, and T. Wriedt (Universidade de Vigo, Vigo, 1999), pp. 273–280.
- [45] C. Hafner, in *Generalized Multipole Techniques for Electromagnetic and Light Scattering*, edited by T. Wriedt (Elsevier, Amsterdam, 1999), pp. 21–38.
- [46] M. Loncar, J. Vuckovic, and A. Scherer, *J. Opt. Soc. Am. B* **18**, 1362 (2001).
- [47] H. Benisty, *J. Appl. Phys.* **79**, 7483 (1996).
- [48] Y. Xu, R.K. Lee, and A. Yariv, *J. Opt. Soc. Am. B* **17**, 387 (2000).
- [49] H.A. Haus, *Waves and Fields in Optoelectronics* (Prentice-Hall, Englewood Cliffs, NJ, 1984).
- [50] C. Manolatu, M.J. Khan, S. Fan, P.R. Villeneuve, H.A. Haus, and J.D. Joannopoulos, *IEEE J. Quantum Electron.* **35**, 1322 (1999).
- [51] Y. Xu, Y. Li, R.K. Lee, and A. Yariv, *Phys. Rev. E* **62**, 7389 (2000).
- [52] C. Hafner and L. Bomholt, *The 3D Electrodynamic Wave Simulator—3D MMP Software and User's Guide* (Wiley, Chichester, 1993).
- [53] It is worth comparing the results shown in Fig. 9 with those obtained with FDTD (Ref. [7] Fig. 2). The method presented here uses a simulation domain of  $15 \times 15$  lattice constants, whereas with FDTD the domain size was  $100 \times 120$  lattice constants. Here, the results deteriorate for  $\omega a / (2\pi c) < 0.325$ , whereas with FDTD spurious oscillations occur for  $\omega a / (2\pi c) < 0.360$ . Despite the large simulation domain employed there, transmission coefficients up to 1.20 for low wave numbers were displayed in Fig. 2 of Ref. [7].